NUMERICAL MODELING OF THE CONSTRAINT EFFECTS ON CLEAVAGE FRACTURE TOUGHNESS

SUNIL PRAKASH, XIAOSHENG GAO AND **T. S. SRIVATSAN**
Department of Mechanical Engineering
The University of Akron
Akron, Ohio 44325
xgao@uakron.edu, tss1@uakron.edu

Abstract: Cleavage fracture has been an important subject for engineers primarily because of its catastrophic nature and consequences. Experimental studies of cleavage fracture did reveal a considerable amount of scatter and provided evidence of noticeable constraint effects. This did provide the motivation for the development of statistical-based and micromechanics-based methods in order to both study and analyze the problem. The Weibull stress model, which is based on the weakest link statistics, uses two parameters (m and σ_u) to effectively describe the inherent distribution of the micro-scale cracks once plastic deformation has occurred and to concurrently define the relationship between the macro-scale and micro-scale driving forces for cleavage fracture. In this paper, we present the results of a recent study at evaluating the constraint effects on cleavage fracture toughness. This was done numerically using a constraint function (g(M)) derived from the Weibull stress model. The non-dimensional function (g(M)) describes the evolution of constraint loss effects on fracture toughness relative to the reference plane-strain, small scale yielding (SSY) condition (T-stress = 0). We performed detailed finite element analyses of single-edge notched bending specimens and computed the non-dimensional g(M) functions for them. The g(M) function varies with (i) the Weibull modulus, (ii) material flow properties, and (iii) specimen geometry, but not with absolute size of the test specimen. Knowing the g-function, the fracture driving force curve can be constructed for each absolute size of interest.

1.   INTRODUCTION

Failure from fracture can occur for many reasons, to include uncertainties arising from the following: (a) loading and/or the environment, (b) defects in the material, (c) inadequacies in design, and (d) deficiencies in construction or maintenance, to name a few. Failure of load-bearing components can be catastrophic, so fracture is a desirable and important consideration for engineers in attempting to design large-scale structures, such as, automobiles, airplanes, power plants and bridges.

In ferritic steels, a large amount of scatter was consistently revealed by the macroscopic values of fracture toughness (J_c, K_{Jc}), when measured experimentally over the lower end of the ductile-to-brittle transition (DBT) range (Wallin, 1984; Sorem, 1991). In the presence of significant plastic deformation along the crack front and in this temperature range, the transgranular cleavage is conducive for the promotion of brittle

---

fracture.   To convincingly describe the observed scatter while being consistent with common observations of single carbide that initiates cleavage along the crack front, models generally adopt the weakest link approach (Beremin, 1983; Wallin, 1984; Lin, 1986). The fracture process is driven by the volume of highly stressed material ahead the crack front. Specimen/component geometry, size, loading mode (e.g. tension versus bending) and material flow properties do exert a profound influence on the elastic-plastic stress fields at the crack front. The interaction of the plastic regions ahead of the crack front with nearby traction free boundaries breaks down the single parameter characterization of the crack front stresses, in terms of the *J*-integral (Rice, 1968).

A complex (nonlinear) relationship between the three-dimensional crack front stresses, the applied *J*-value, which varies along the crack front, and the corresponding stressed volume of material at the crack front drives the weakest link mechanism (Moinereau, 1996; Weisner, 1996; Ruggieri, 1998; Gao, 1998). In an attempt to mitigate these complexities, testing standards for the measurement of cleavage fracture toughness in the DBT range (ASTM E1921, 1998) require selection of the specimen type, size, and loading mode to ensure that essentially plane strain, small-scale yielding (SSY) conditions exist along the crack front at the time of fracture. The commonly used specimens include: (a) the single-edge notched bending specimens (SE(B)), and (b) the compact tension specimens (C(T)) with crack length (or depth) (*a*) to specimen width (*W*) ratios, $a/W \geq 0.5$. However, even these deep-notch geometries eventually lose the small-scale yielding (SSY) condition at large *J*-values (Mudry, 1989). Therefore, the deformation limits of the form $M = b\sigma_0/J_c > M_{limit}$ were imposed on the testing standards.   In this expression, *b* denotes the length of the remaining ligament, σ_0 represents the yield stress and M_{limit} defines the non-dimensional deformation limit.

The values specified for M_{limit} are important for delineating the minimum allowable specimen size for material testing. The test standard ASTM E1921, specifies M_{limit} to be equal to 30. The Charpy size specimens can be tested from this value in the lower transition region for common structural and pressure vessel steels. The $M_{limit} = 30$ value was selected based on an experimental basis. Three-dimensional finite element analyses of the single-edge notch (SE(B)) and compact tension (C(T)) specimens by Nevalainen and co-workers (1995) suggest $M_{limit} \approx 60$–80 for the purpose of maintaining small-scale yielding (SSY) conditions on the center plane for moderately hardening materials.

For testing small specimens having low *M* values at fracture, a suitable deformation limit becomes significant. For example, to assess the integrity of the pressure vessel of a nuclear power plant, one needs to test sub-size specimens because of limited availability of material (material extracted from surveillance capsules). However, these sub-size specimens are difficult for the purpose of the following the ASTM standard E1921. Hence, this calls for a toughness scaling model to be developed, such that the test results on a standard SE(B) specimen can be scaled to sub-sized specimens.

In this paper, we focus on investigating the constraint loss effects using the constraint function, *g(M)*, proposed by Gao and Dodds (2000) based on the Weibull stress model (Beremin, 1983). We study the nonlinear response of a series of SE(B) specimens having crack length to specimen width ratios of $a/W = 0.1$ and 0.5, specimen

width to thickness ratios of $W/B = 1$ and 2, and with or without side grooves (20% side-grooves: 10% each side) and compute the constraint function $g(M)$ for each of them. The parametric study considers three sets of material flow properties for (i) $n = 5$, 10 and 20, where n represents the strain hardening exponent, and (ii) $E/\sigma_0 = 800$, 500 and 300, where E is the Young's modulus. This selection on n and E/σ_0 represents a wide range of ferritic steels. Effects of scatter in local toughness values were incorporated into the analysis by varying the Weibull modulus for $m = 8$, 12, 16 and 20. We attempt to introduce the applied load by rollers, which are in contact with the specimen (realistically represents the actual experimental set-up), thereby the anticlastic bending effect can be captured. The results demonstrate the strong constraint effect on cleavage fracture toughness and how different parameters influence this effect.

2.   WEIBULL STRESS MODEL

In ductile-to-brittle transition (DBT) region, fracture specimens fail by transgranular cleavage in the presence of significant plasticity. Transgranular cleavage fracture develops from slip-induced cracking of carbides, generally located at and along the grain boundaries, followed by unstable propagation of the resultant cracks into the surrounding ferrite matrix (McMohan, 1965). Experimental studies have convincingly shown that the process becomes strongly driven by a single critical cleavage event at the metallurgical scale that triggers macroscopic brittle fracture (Hahn, 1984; Wang, 1991).

Due to microstructural inhomogeneity of the material, such as, carbide particle distribution, carbide particle shape, and carbide particle orientation, volume sampling effects play an important role to quantify the large, observed scatter in fracture toughness data measured in the transition region. When constraint levels vary under increased loading (for example, due to the influence of nearby traction free boundaries on crack-front plastic zones), single parameter characterization (using J) breaks down and there develops a complex, nonlinear interaction between the constraint levels and the probabilistic modeling.

In the local approach to model cleavage fracture, the probability distribution (P_f) for fracture stress of a cracked solid at a global load level K_J or J has been shown to follow a two-parameter Weibull distribution (Beremin, 1983; Mudry, 1987; Minami, 1992) of the form

$$P_f(\sigma_w) = 1 - \exp\left[-\frac{1}{V_0}\int_{\overline{V}}\left(\frac{\sigma_1}{\sigma_u}\right)^m dV\right] = 1 - \exp\left[-\left(\frac{\sigma_w}{\sigma_u}\right)^m\right] \qquad (1)$$

In this expression $\overline{V}$ denotes the volume of the cleavage fracture process zone, V_0 defines a reference volume for dimensional correctness and σ_1 is the maximum principal stress acting on material points inside the fracture process zone (i.e., the plastic zone). Parameters m and σ_u in Equation (1) define the Weibull modulus and the scale parameter of the Weibull distribution. The Weibull modulus is related to size distribution of the microscopic cracks and the scale parameter helps in characterizing the micro-scale fracture toughness.

Equation (1) was derived by Beremin (1983) based on the weakest link statistics, which introduces a local fracture parameter, the Weibull stress (σ_w)

$$\sigma_w = \left[\frac{1}{V_0} \int_V \sigma_1^m \, dV \right]^{1/m} \tag{2}$$

The Weibull stress provides a local crack-front parameter that serves to couple remote loading with a micromechanics model that incorporates the statistics of microcracks. Under increased remote loading described by K_J or J, intrinsic differences in the evolution of Weibull stress (σ_w) reflect the strong variation in crack-front stress fields arising from the effects of constraint loss and volume sampling. The inherently three-dimensional formulation for σ_w defined by Equation (2) readily accommodates variations in K_J or J along the crack front.

Under the plane-strain, small-scale yielding (SSY) conditions, the volume of the cleavage process zone (i.e., plastic zone) scales with thickness $(B) \times J^2$. The relationship between σ_w and J leads to a simpler form (Gao et. al., 1998)

$$\sigma_w^m = \varsigma \, B \, J^2 \tag{3}$$

In this equation ς denotes a constant that depends only on the material flow properties (E/σ_0, υ, and n) and the Weibull model parameters (m and V_0). B is the thickness of the test specimen.

For three-dimensional fracture specimens, the stress and deformation fields vary over the thickness. Generally, the mid-plane stresses have the largest values with sharp reductions at the traction-free outside surfaces. Thus, the contribution to Weibull stress (σ_w) from each material point in the thickness direction can vary significantly. Consequently, the simple effect of specimen thickness on cleavage probability suggested by Equation (3) no longer applies. To quantify the non-uniformity of stress and deformation fields along the crack front direction (Z-direction), Gao and Dodds (2000) introduced a Weibull stress density function, $\overline{\sigma}_w$, such that $\sigma_w^m = \int_{-B/2}^{B/2} \overline{\sigma}_w^m(Z) \mathrm{d}Z$. Dimensional analysis suggests, and numerical experiments confirm, that $\overline{\sigma}_w^m = \varsigma J^2 f(M, s)$, where $s = Z/(B/2)$ denote the non-dimensional location of a point on the crack front, and the function $f(M, s)$ remains the same for all geometrically similar specimens for a given material. As a result,

$$\sigma_w^m = \varsigma \, B \, J^2 \int_{-1}^{1} f(M, s) \mathrm{d}s = \varsigma \, B \, J^2 \, g(M) \tag{4}$$

Equation (4) defines a non-dimensional constraint function, $g(M)$, that characterizes the amount of constraint loss once SSY conditions degenerate in specimens under increased plastic deformation. The constraint function equals to 1.0 for all materials under plane-strain, SSY conditions with $T = 0$. For a specific specimen configuration, 3D non-linear finite element analyses and Weibull stress computations produce the σ_w versus J_{avg} (through-thickness average J) results. With the ς value determined from the SSY solution, the value of the g can be calculated from Equation (4) at each deformation level.

3.   THE NUMERICAL MODEL

3.1 Finite element model

Non-linear finite element analyses were performed using MSC/Patran (2005) for meshing, loading and ABAQUS/Standard (2007) for solving. Various configurations of

the single-edge notched bending specimens (SE(B)) were studied. Each fracture model consisted of three-dimensional, 8-node hexahedral elements with full integration $2\times2\times2$ gauss quadrature. Use of the hybrid formulation helps minimize the volumetric locking as the deformation progress into the fully plastic, incompressible mode. The J-integrals were evaluated using a domain integral procedure with the domains defined outside of the material experiencing severe element distortion. The computed J-values exhibit domain independence. ABAQUS computes the J-value at each crack front node location at each loading increment. The average J-value through the thickness provides a convenient parameter to characterize the average intensity of far-field loading on the crack front and therefore, the J-values obtained from ABAQUS are averaged along the crack front.

3.2   Constitutive model

The material model employed in the parametric studies follows a J_2 flow theory with conventional Mises plasticity. The finite element computations were performed within the finite-strain framework. The uniaxial true stress-logarithmic strain curve obeys a simple power-law hardening model preceded by a purely linear response prior to plastic flow,

$$\frac{\varepsilon}{\varepsilon_0} = \frac{\overline{\sigma}}{\sigma_0} \quad for \quad \varepsilon \leq \varepsilon_0 ; \qquad\qquad \frac{\varepsilon}{\varepsilon_0} = \left(\frac{\overline{\sigma}}{\sigma_0}\right)^n \quad for \quad \varepsilon > \varepsilon_0 \qquad (5)$$

Where in this expression σ_0 is the yield stress, ε_0 is the yield strain, and n is the strain hardening exponent. A user defined subroutine (UHARD) was used to implement this material model into ABAQUS. Computational results are presented for the following three cases: (i) a strongly hardening material ($E/\sigma_0 = 800$, $n = 5$) characteristic of civil and marine structural steels, (ii) a moderately hardening material ($E/\sigma_0 = 500$, $n = 10$) characteristic of many pressure vessel and pipelines steels, and (iii) a very low hardening material ($E/\sigma_0 = 300$, $n = 20$). For all computations the Poisson's ratio υ was taken to be equal to 0.3.

3.3   Three-Dimensional (3-D) Finite Element Model for the SE(B) specimen

Non-linear finite deformation analyses was performed on a series of geometries:
(i)   Plane-sided SE(B) specimens with $a/W = 0.1$ and 0.5, $W/B = 1$ and 2, and
(ii)   Side-grooved (10 percent each side) SE(B) specimens with $a/W = 0.1$ and 0.5, $W/B = 1$ and 2.

Here a represents the crack length, W represents the specimen width and B represents the specimen thickness. A mesh configuration having $30 - 50$ focused rings of elements in the radial direction surrounds the crack front (see Figure 1-2). The crack tip has a small, initial radius (see Figure 3) to facilitate enhancing convergence of the finite-strain solutions. Under increased loading, extensive distortion of the element at the notch root prevents convergence of the global Newton iterations. Therefore, several different meshes were employed for each specimen with increasingly larger initial root radius. A recent study by Gao and Dodds (2000) has revealed that there will be no effect of initial root radius on stress distribution ahead of the crack-tip once $\rho/\rho_0 > 2.5$; where ρ_0 is the initial root radius ρ is the deformed root radius. To limit the effect of the initial root radius (ρ_0) on the Weibull stress calculations, the analyses use finite element models having three different root radii of 1.2 μm, 2.5 μm and 5 μm. The model with the smallest

root radius provides Weibull stress results early in the loading history at relatively low *J*-values. At the larger *J*-values, element distortions along the crack front reach unacceptable levels using this model. The second model, having larger initial root radius permits loading to much higher *J*-values. At intermediate *J*-values, all the models essentially generate identical results, providing a verification of this strategy. For all specimen sizes, meshes in the crack front region have a fixed element density. This eliminates possible near-front meshing effects as size of the specimen increase.

Due to symmetry, only a quarter of the specimen needs to be meshed. The mesh having 15 – 16 variable thickness layers defined over the half-thickness. The thickest layer lies at $Z = 0$ while the thinner layers were defined to be near the free surface ($Z = B/2$) to accommodate strong Z variations in the stress distribution. The quarter-symmetric 3-D SE(B) specimen having a deep-crack contains 32,200 elements to 26,000 elements based on different initial crack-tip radius, whereas for a specimen having a shallow crack 24,600 elements to 20,000 elements based on different initial crack-tip radius.

We apply displacement boundary condition to the finite element model by defining frictionless contact between the rigid rollers and the specimen; one being the loading roller while the other is the support roller (see Figure 1). The reference node of each of the roller has prescribed displacement, transverse displacement is given to the loading roller and all other directions set to zero and for the support roller all the direction are set to zero. At load levels well beyond the formation of plastic hinge, the outermost nodes develop a small uplift (tension) force showing presence of anticlastic bending (Gao and Dodds, 2000).
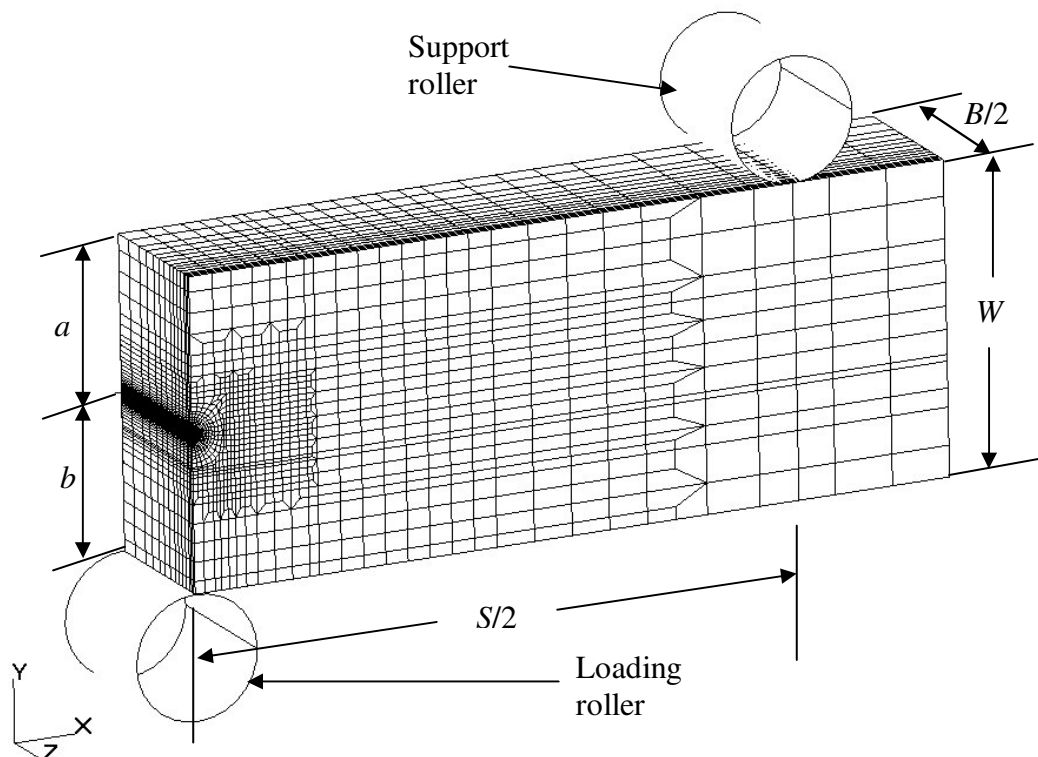

Figure 1.   Quarter-symmetric finite element model for a plane-sided SE(B) specimen
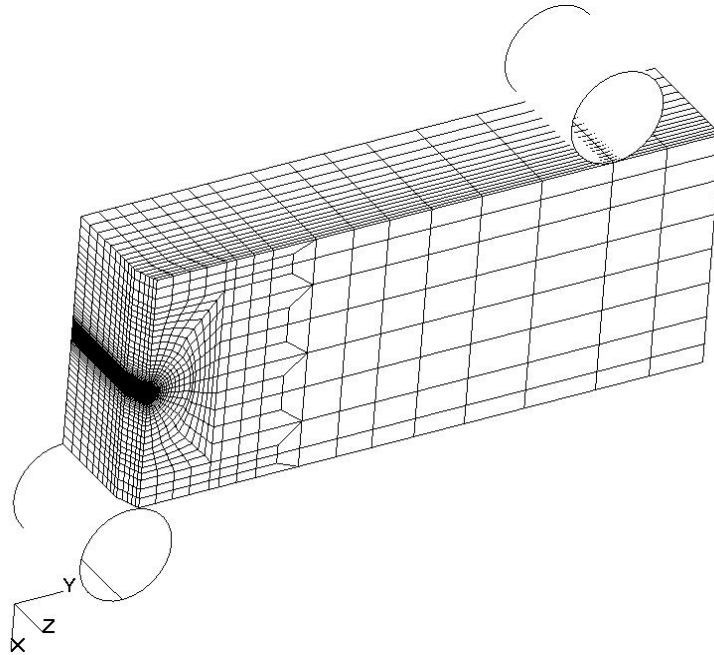
Figure 2.   Quarter-symmetric finite element model for a side-grooved SE(B) specimen

3.4   The Small Scale Yielding model (SSY)

The plane-strain, SSY ($T = 0$) stress fields define a high constraint, reference crack-front condition for the purpose of assessing constraint loss for three-dimensional geometries. This study makes use of a boundary layer model (Larrson, 1973; Rice, 1974) where the plastic zone remains small compared to the outer boundary radius (see Figure 3).   Under the plane-strain, SSY conditions, the local J as well as the stress and deformation fields remain identical at each crack front location over the thickness. This idealized model defines a severe constraint level that is attainable in the real fracture specimens only at low loading levels. This reference condition is used to interpret the three-dimensional results.

With the plastic region limited to a small fraction of the domain radius (R) included in the model ($R_p < R/20$), the general form of the asymptotic crack-tip stress fields in the region well outside of the plastic region is given by (Williams, 1957)

$$\sigma_{ij} = \frac{K}{\sqrt{2\pi r}} f_{ij}(\theta) + T\,\delta_{1i}\,\delta_{1j} \tag{6}$$

In this equation K is the stress intensity factor $f_{ij}(\theta)$ defines the angular variations of in-plane stress components, and the non-singular term T represents a tension (or compression) stress parallel to the crack plane. Numerical solutions for $T = 0$ are generated by imposing displacements of the elastic, Mode I singular field on the outer circular boundary ($r = R$) that encloses the crack

$$u(R,\theta) = K\frac{1+\upsilon}{E}\sqrt{\frac{R}{2\pi}}\,\cos(\frac{1}{2}\theta)(3-4\upsilon-\cos\theta) \tag{7}$$

$$v(R,\theta) = K\frac{1+\upsilon}{E}\sqrt{\frac{R}{2\pi}}\,\sin\,(\frac{1}{2}\theta)(3-4\upsilon-\cos\theta) \tag{8}$$

The SSY model used for analysis (see figure 3) has one layer of 2,770 three-dimensional elements with plane-strain constraints ($w = 0$ imposed at all nodes). Under the plane strain, SSY conditions $J = K^2 (1-\upsilon^2)/E$.

By coupling the finite element results for the SSY model with Equation (3), accurate values of the Weibull stress can be obtained for any loading level (J) in SSY. The constant ς in Equation (3) can be calculated for a given m and applied J value obtained from ABAQUS. Finite element results are used once the deformed root radius exceeds $2.5\times$ the initial radius. This scheme minimizes the effects of initial notch root radius and near tip meshing. Simple scaling of the SSY Weibull stress values to the thickness of a SE(B) specimen as provided by Equation (3) provides values for an assessment of the loss in constraint.
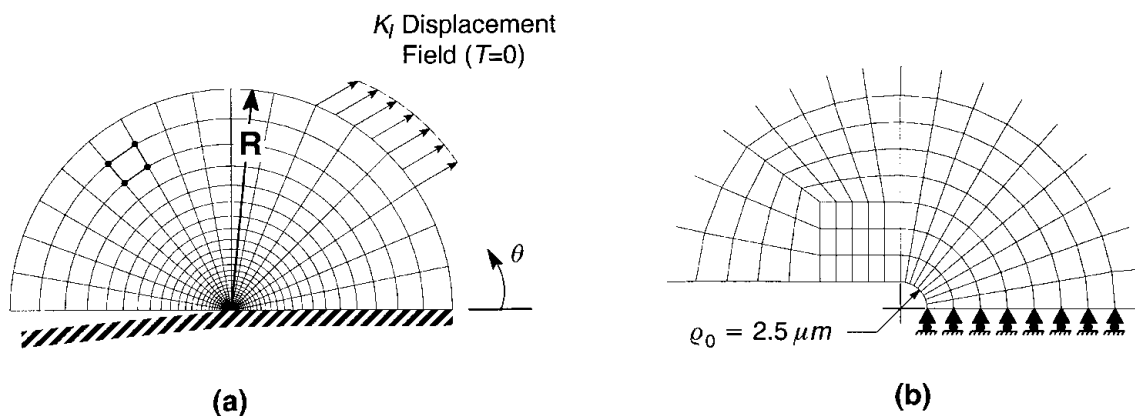
Figure 3.   **(a)**   **The small-scale yielding (SSY) model.**
                 (b)   **Near-tip mesh, where the initial root radius is 2.5 μm**

3.5   Numerical computation of the Weibull stress

Numerical evaluation of the Weibull stress, defined by Equation (2), using the finite element results proceeds as follows. Let $|J|$ denote the determinant of the standard coordinate Jacobian between the deformed Cartesian coordinates x_i and the parametric coordinates η_i. Using standard procedures for integration over element volumes, the Weibull stress takes the form

$$\sigma_w = \left[\frac{1}{V_0}\sum_{n_e}\int_{-1}^{1}\int_{-1}^{1}\int_{-1}^{1}\sigma_1^m\,|J|\,d\eta_1\,d\eta_2\,d\eta_3\right]^{1/m} \tag{9}$$

where n_e is the number of elements inside the fracture process zone. The process zone includes all material points that experience plastic deformation. This expression for the Weibull stress represents an integral form in parametric space of Beremin's formulation (Beremin, 1983). A post-processing program is developed in FORTRAN to compute the Weibull stress using the finite element results of ABAQUS.

The reference volume (V_0) is taken to be 1 mm³ for purpose of convenience in all calculations. As Equation (1) indicates, the Weibull stress scales with this reference volume. A change of the reference volume from V_0 to $\overline{V}_0$ requires scaling of σ_u to $\overline{\sigma}_u$ such that $V_0 \times \sigma_u^m = \overline{V}_0 \times \overline{\sigma}_u^m$ maintaining identical failure probabilities.

4.   NUMERICAL RESULTS

This section describes key results derived from detailed three-dimensional finite element analyses of the SE(B) specimens. The through-thickness average value of J quantifies the level of applied loading. The non-dimensional parameter $M = b\sigma_0 / J_{avg}$ defines the loading level scaled to the specimen size (b denotes the remaining ligament length).

The non-dimensional constraint function ($g(M)$) depends on the material flow properties and the Weibull modulus, but not on the absolute size of the specimen. Larger values of $g(M)$ indicate higher levels of crack front constraint. For the plane strain, SSY configuration ($T = 0$), $g(M) = 1.0$ regardless of material properties. For the fracture specimens, $g(M)$ decreases as deformation progresses as a result of constraint loss and the deformation level (M) at which $g(M)$ falls below unity depends on both material flow properties and the Weibull modulus.

Knowing the non-dimensional constraint function ($g(M)$) for a specimen geometry enables construction of the σ_w versus J curves (fracture driving force curve) for all geometrically similar specimens without additional finite element analyses. For example, by modeling a 1T SE(B) specimen (thickness = 25mm) with $B = W$, $S = 4W$ and $a/W = 0.5$, the generated non-dimensional constraint function $g(M)$ remains valid for all SE(B) specimens having sizes proportional to this 1T specimen. The parameter study described here considers three sets of material flow properties, $n = 5$, 10 and 20 having strengths $E/\sigma_0 = 800$, 500 and 300 respectively, which represents a wide range of ferritic steels. Effects of scatter in the local toughness values enter the simulations by varying the Weibull modulus with $m = 8$, 12, 16 and 20.

A single set of finite element analyses of a 1T specimen generates the constraint function $g(M)$ for each different set of material flow properties. Each set of the analyses uses three models that differ in size of the initial root radius, namely: (a) 1.2 μm, (b) 2.5 μm, and (c) 5 μm (refer to section 3.3). The smaller radius model provides the Weibull stress values early in the loading. At the higher loading levels, the larger radius model becomes necessary to avoid excessive distortion of the mesh at the crack front. In both cases, the numerical results are considered valid only when the deformed root radius exceeds $2.5 \times$ the initial radius.

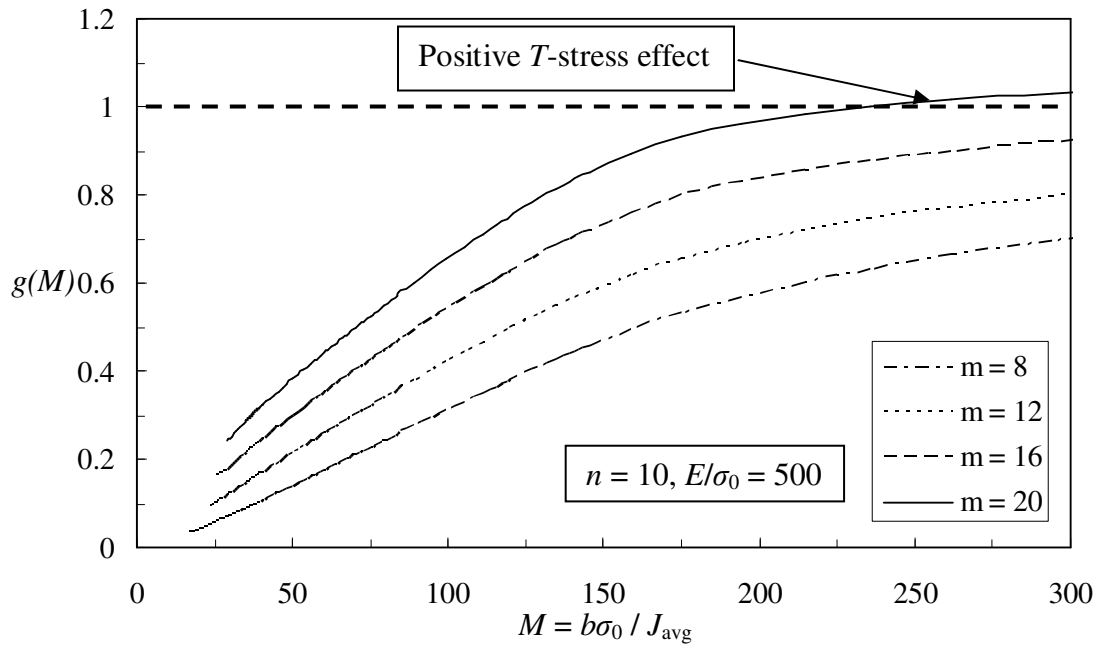### 4.1   Effect of different material properties on constraint loss $g(M)$

Here we consider a plane-sided SE(B) specimen with $a/W = 0.5$, $W = B$ and $S = 4W$. In Figures 4-6 is shown the computed $g(M)$ function for each of the three material property sets. The g-function describes the evolution of constraint loss over the loading history relative to the plane-strain SSY reference condition (zero T-stress). When the small scale yielding condition no longer prevails in the specimens under increased plastic

deformation, the *g*-function values fall well below 1.0 capturing the complex relationship between Weibull stress, local crack-front stress and average value of *J* integral across the crack-front. At low load levels (*M* > 200), portions of the *g*-function curves generally lie above 1.0 for the larger *m* values. This behavior is due to the positive *T*-stress inherent in deep-notch SE(B) geometry. The positive *T*-stress raises the Weibull stress above the SSY (*T* = 0) value until constraint loss from an increase in plastic deformation eventually causes the crack-front stresses and the Weibull stress (σ_w), to fall below SSY levels, leading to *g(M)* < 1.0. The smaller *m* values cause *g(M)* to drop below 1.0 even at the low load levels since they increase the relative contribution to σ_w from the lower stressed material situated at greater distance from the crack-front and near the free surface.

The *n* = 10 and *n* = 20 material shows more constraint loss at higher deformation levels whereas *n* = 5 shows less loss of the constraint. The *n* = 10 material with *m* = 20, shows positive *T*-stress (*T* > 0) effect. For *n* = 5 material with *m* = 20, we need a smaller crack tip radius mesh to capture the constraint loss in lower deformation level (i.e., higher values of *M*). When plastic deformation increases the constraint function (*g(M)*) decreases. For deformation *M* < 100, we see a severe loss of the constraint in each of the material sets.
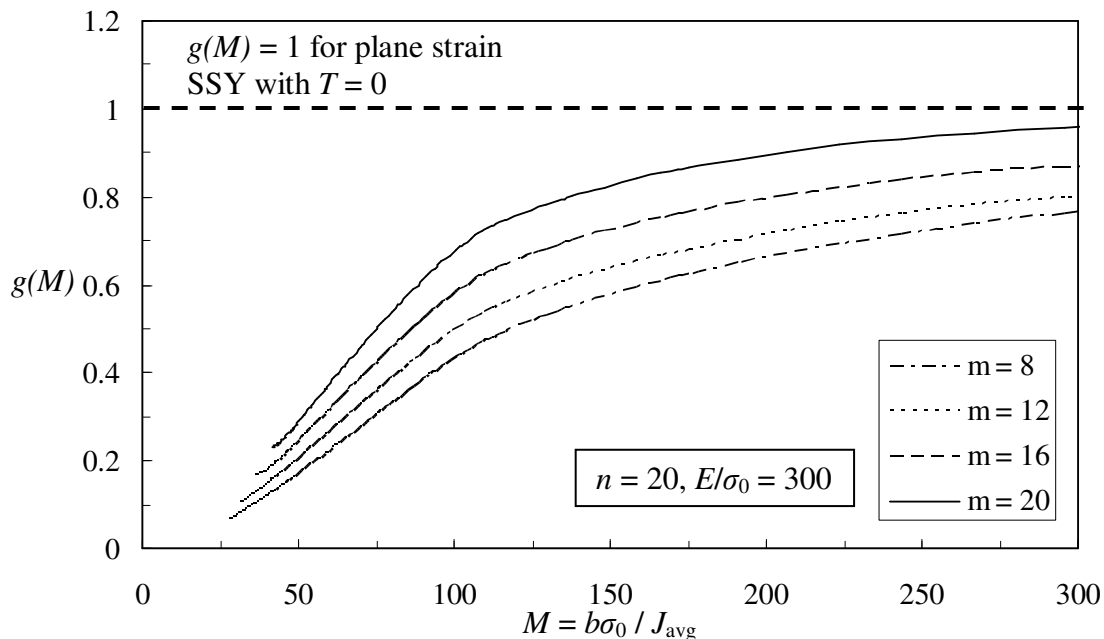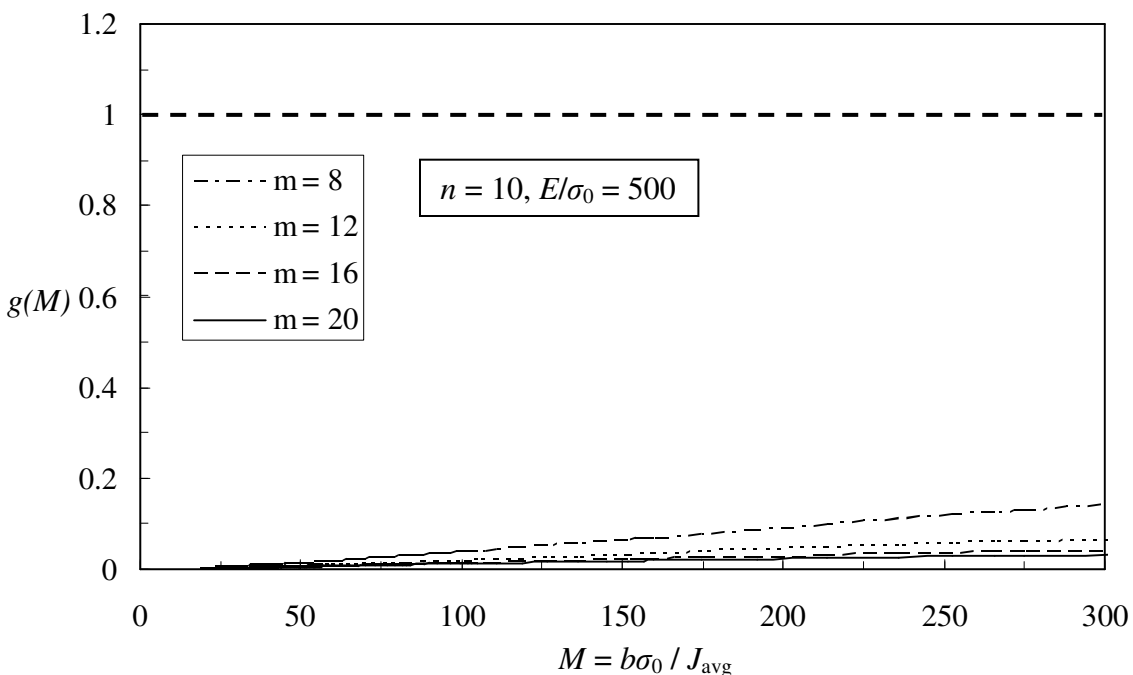

Figure 4.   **The non-dimensional constraint function, *g(M)*, for square cross-section SE(B) specimens. The material flow properties are *n* = 20, *E*/σ_0 = 300 and *v* = 0.3**

Figure 5. The non-dimensional constraint function, *g(M)*, for square cross-section SE(B) specimens. The material flow properties are *n* = 10, *E/σ₀* = 500 and *v* = 0.3
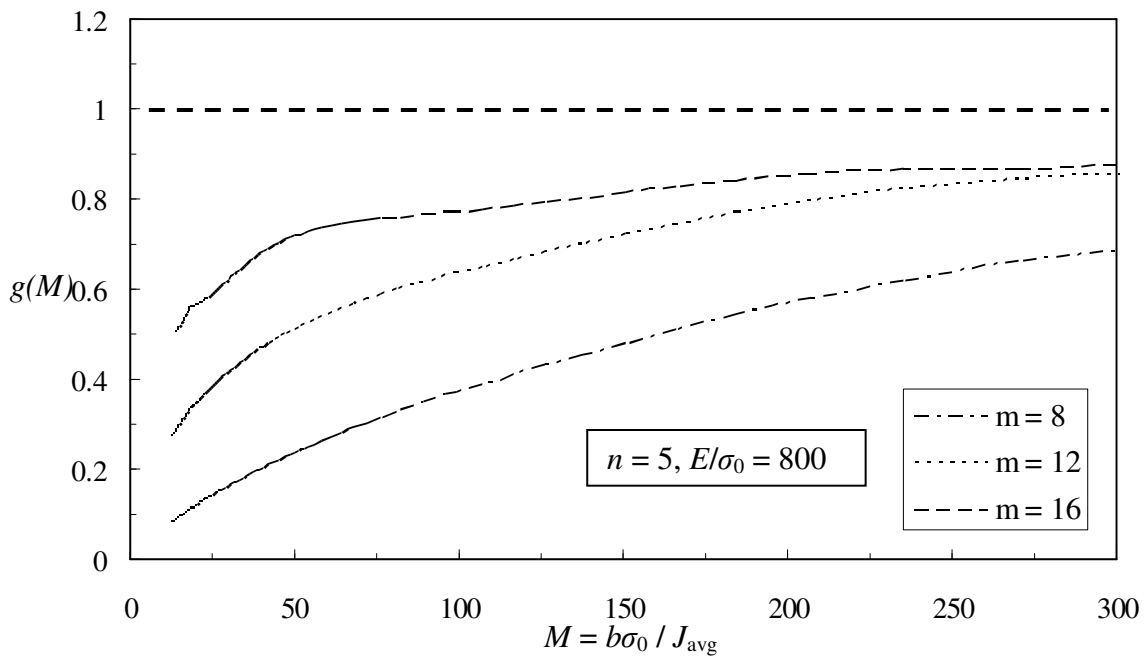
Figure 6. The non-dimensional constraint function, *g(M)*, for square cross-section SE(B) specimens. The material flow properties are *n* = 5, *E/σ₀* = 800 and *v* = 0.3

## 4.2   Effect of different crack-length on the constraint loss *g(M)*

Here, we consider a plane-sided SE(B) specimen with $a/W = 0.1$, $W = B$ and $S = 4W$ for the $n = 10$, $E/\sigma_0 = 500$ and $\upsilon = 0.3$ material. In Figure 7 is shown the computed constraint function *g(M)*. The shallow cracked specimens show very low constraint levels and also the constraint curves for different Weibull modulus *m* are very close indicating a smaller effect of the parameter *m*. Comparing Figure 5 and Figure 7, i.e., $a/W = 0.5$ (deep crack) and $a/W = 0.1$ (shallow crack), we observe the a/W ratio to strongly affect the constraint level (the shallow crack specimen shows very low constraint levels when compared to the deep crack specimen).

## 4.3   Effect of different cross-sections on the constraint loss *g(M)*

Here we consider a plane-sided SE(B) specimen with $a/W = 0.5$, $W = 2B$ and $S = 4W$ for the $n = 10$, $E/\sigma_0 = 500$ and $\upsilon = 0.3$ material. Figure 8 shows the computed *g(M)* function. The constraint loss increases once the deformation level goes beyond $M < 150$. The smaller values of *m* show lower constraint level since they increase the relative contribution to Weibull stress from lower stressed material. Comparing Figure 5 and Figure 8, i.e., $W = B$ (square cross-section) with $W = 2B$ (rectangular cross-section), we do observe that the square cross-section shows higher constraint levels than the rectangular cross-section.

Figure 7.   **The non-dimensional constraint function, *g(M)*, for square cross-section SE(B) specimens. The material flow properties are *n* = 10, *E/σ₀* = 500 and *υ* = 0.3**
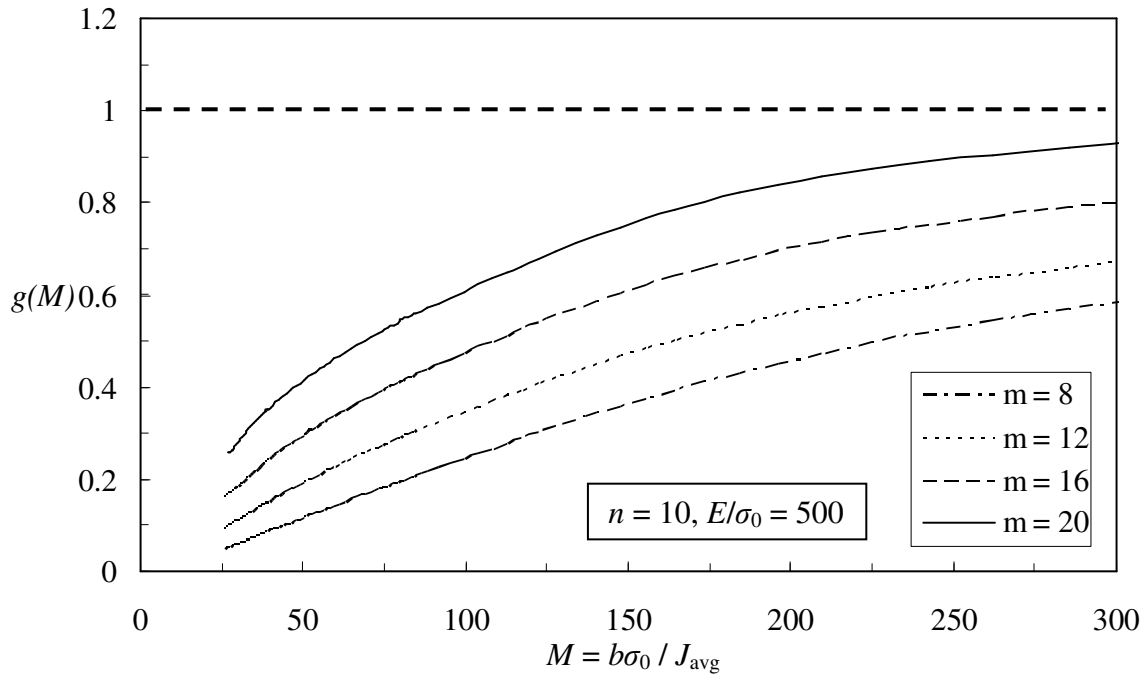
Figure 8. The non-dimensional constraint function, *g(M)*, for rectangular cross-section SE(B) specimens. The material flow properties are *n* = 10, *E/σ₀* = 500 and *υ* = 0.3
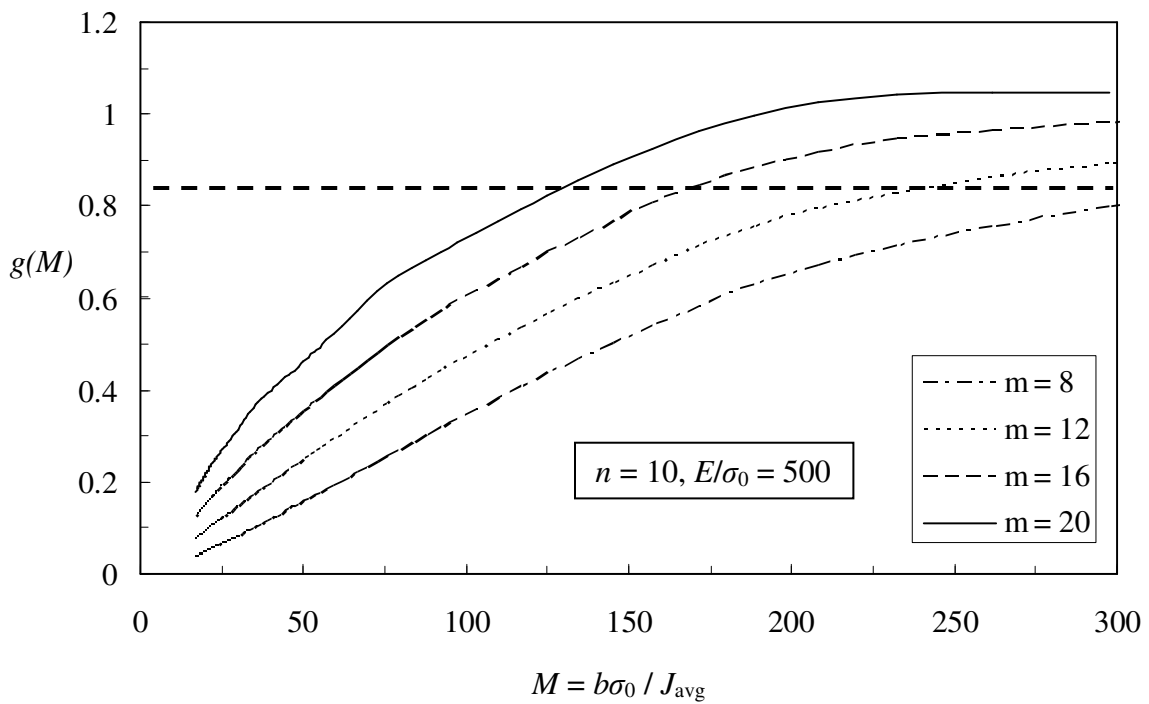

Figure 9. The non-dimensional constraint function, *g(M)*, for side-grooved, square cross-section SE(B) specimens. The material flow properties are *n* = 10, *E/σ₀* = 500 and *υ* = 0.3

4.4   Effect of side-grooved and no side-groove specimen on constraint loss *g(M)*

In this study we consider a SE(B) specimen with $a/W = 0.5$, $W = B$, $S = 4W$ and having side-grooves (20% of thickness) for a material having $n = 10$, $E/\sigma_0 = 500$ and $v = 0.3$. . In Figure 9 is shown the computed *g(M)*. Comparing Figure 5 and Figure 9, i.e., plane-sided specimen and side-grooved specimen, we observe the side-grooves increase the constraint levels.

4.5   Discussions

The specimens are loaded using a rigid roller by defining frictionless contact instead of directly applying nodal displacements on specimen surface provided evidence of the anticlastic bending effect away from the center plane. The nodes away from the center plane experienced zero load, i.e., the specimen was no longer in contact with the roller due to the anticlastic bending. Let $s = Z/(B/2)$ denote the non-dimensional location of a point on the crack front. A plot of contact pressure (*P*) versus the non-dimensional location (*s*) is shown in Figure 10. This figure reveals the contact pressure to be maximum at the mid-plane ($Z = 0$) and approaches zero at the surface. The contact pressure approaching zero at the surface indicates the presence of anticlastic bending effect locally near the surface.
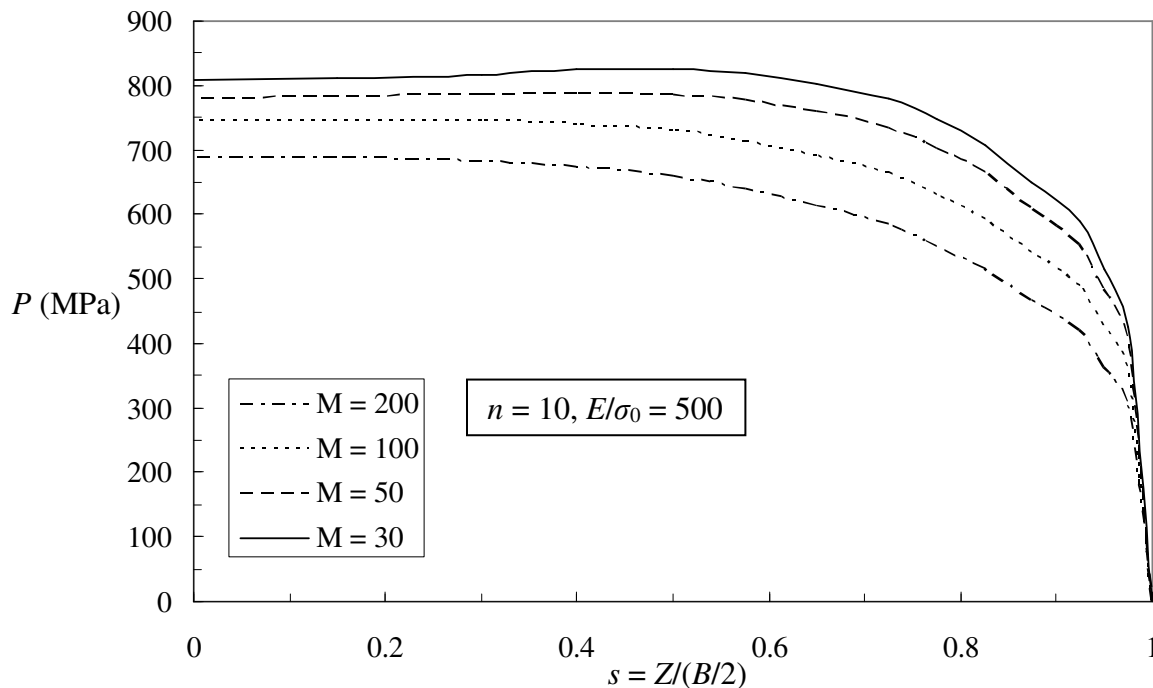

Figure 10.   **Contact pressure distribution at the nodes in contact with loading roller at four deformation levels (*M* = 200, 100, 50, 30) for the *a/W* = 0.5, *W = B*, SE(B) specimen**

Figures 11-12 show the evolution of the Weibull stress density across the crack front under increased loading for a representative Weibull modulus of $m = 8$. For the specimen loaded with rigid frictionless contact is shown in Figure 11, while Figure 12 is for the specimen loaded directly by applying nodal displacement. These plots show the maximum densities to be at the center-plane for all loading levels. Further, we can

observe that the Weibull stress density for the specimen loaded with roller and the specimen with direct load are not much different. Consequently, the fracture driving force predicted by the two models should be almost the same.

$$s = Z/(B/2)$$
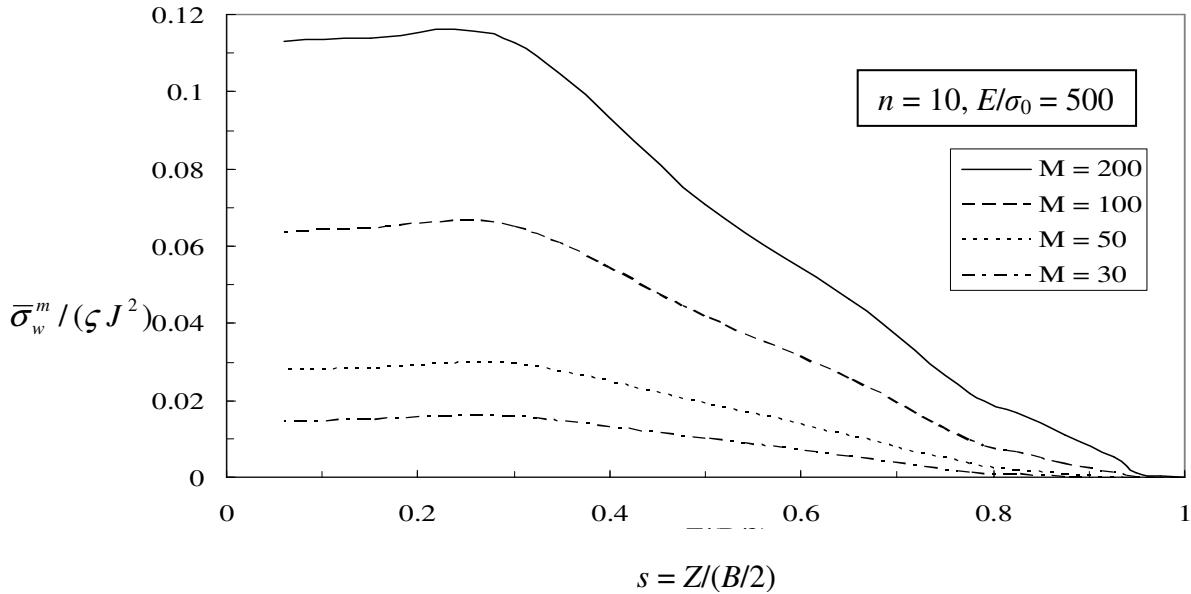
Figure 11. **Normalized Weibull stress density distribution for the *a/W = 0.5*, *W = B*, SE(B) specimen loaded through roller at four deformation levels (*M* = 200, 100, 50, 30), where the Weibull modulus *m* = 8**

$$s = Z/(B/2)$$
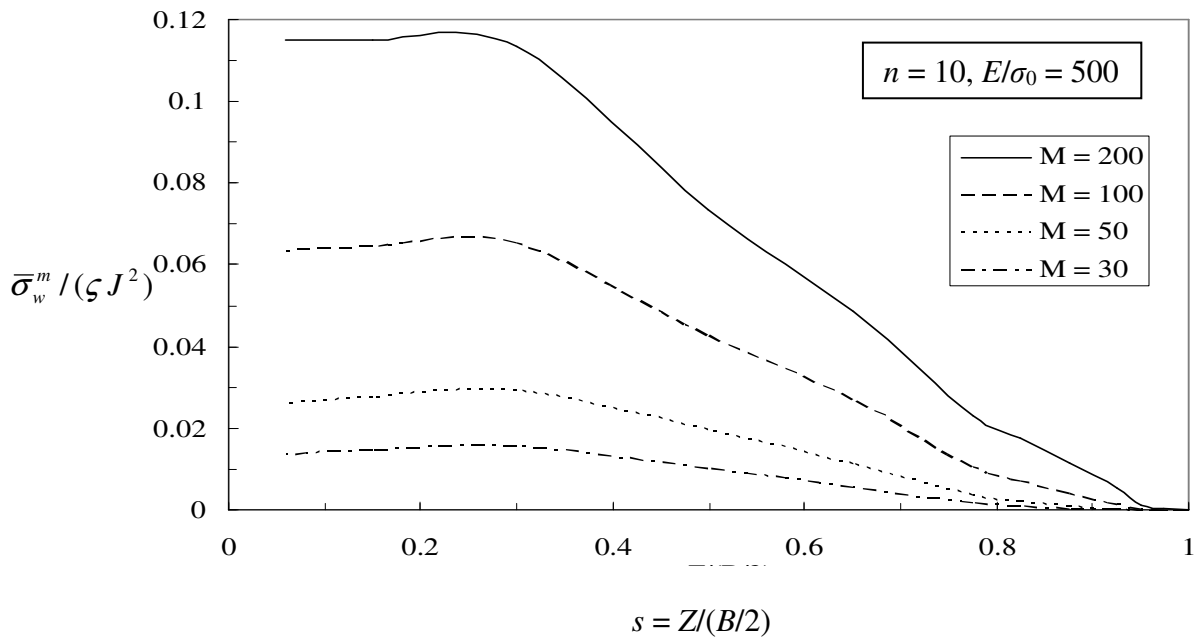
Figure 12. **Normalized Weibull stress density distribution for the *a/W = 0.5*, *W = B*, SE(B) specimen by direct displacement loading at four deformation levels (*M* = 200, 100, 50, 30), where the Weibull modulus *m* = 8**

5.   CONCLUSIONS

For a given type of specimen and a specific material, the non-dimensional function, $g(M)$, defines constraint evolution. Larger values of $g(M)$ imply higher levels of constraint; $g(M) = 1.0$ for plane strain, SSY (with T-stress = 0), while for the SE(B) specimens, $g(M)$ decreases as deformation level increases.

The g-function remains identical for all geometrically similar specimens regardless of their absolute sizes. Knowing the g-function for a specimen geometry enables construction of the fracture driving force curves (σ_w versus J) for all geometrically similar specimens of the same material without additional finite element analysis.

The $n = 5$ material shows less constraint loss than the materials having $n = 10$ and $n = 20$. The a/W ratio greatly affects the Weibull stress (σ_w) and hence the constraint function $g(M)$. As a result, shallow cracked specimens have low Weibull stress (fracture driving force) compared to the deep cracked specimens for the same J-level. Comparing specimens with different W/B ratios, we observe that $W/B = 1$ (square cross-section) shows slightly more constraint than the $W/B = 2$ (rectangular cross-section) for the deep crack configuration. Comparing the side-grooved and plane-sided specimens, we observe higher constraint in the side-grooved specimens than the plane-sided specimens.

For the specimens considered in this study anticlastic bending occurs as deformation increases. However, it has negligible effect on the Weibull stress and hence the constraint function $g(M)$. An absence of this effect is because almost all contributions to the Weibull stress are from layers near the mid-plane, whereas the layers near the free surface have little contribution to the Weibull stress (refer to Figure 11).

REFERENCES

[1] Anderson, T.L. (2005) Fracture Mechanics, Fundamentals and Applications, *CRC press*.

[2] Anderson, T.L and Dodds, R.H. (1991) Specimen size requirements for fracture toughness testing in the ductile-brittle transition region. *Journal of Testing and Evaluation*. 19, 123-134.

[3] American Society for Testing and Materials, Philadelphia. (1998) Test Method for the Determination of Reference Temperature T_0 for Ferritic Steels in the Transition Range (ASTM E 1921).

[4] ABAQUS, V6.7 (2007) ABAQUS reference manuals. 2007. Providence, RI.

[5] Beremin, F.M. (1983) A local criterion for cleavage fracture of a nuclear pressure vessel steel. *Metallurgical Transactions*. 14A, 2277-2287.

[6] Bakker, A and Koers, R.W.J. (1991) Prediction of cleavage fracture events in the brittle-ductile transition region of a ferritic steel. *Defect Assessment in Components-Fundamentals and Applications*, ESIS.EG9 (Edited by Blauel and Schwalbe), Mechanical Engineering Publications, London, 613-632.

[7] Dodds, R.H, Anderson, T.L and Kirk, M.T. (1991) A framework to correlate *a/W* ratio effects on elastic-plastic fracture toughness (J_c). *International Journal of Fracture*. 48, 1-22.

[8] Griffith, A.A. (1920) The phenomena of rupture and flow in solids, *Philosophical transactions*, Series A, 221,163-198.

[9] Gao, X, Ruggieri and Dodds, R.H. (1998) Calibration of Weibull stress parameters using fracture toughness data. *International Journal of Fracture.* 92,175-200.

[10] Gao, X and Dodds, R.H. (2000) Constraint effects on the ductile-to-brittle transition temperature of ferritic steels, a Weibull stress model. *International Journal of Fracture.* 102, 43-69.

[11] Gao, X and Dodds, R.H. (2001) An engineering approach to assess constraint effects on cleavage fracture toughness. *Engineering Fracture Mechanics.* 68, 263-283.

[12] Hahn, G.T. (1984) The influence of microstructure on brittle fracture toughness. *Metallurgical Transactions A.* 15A, 947-959.

[13] Inglis, C.E. (1913) Stress in plate due to the presence of cracks and sharp corners, *Transactions of the Institute of Naval Architects*, 55,219-241.

[14] Koppenhoefer, K and Dodds, R.H. (1997) A three-dimensional numerical investigation of loading rate effects on cleavage fracture of pre-cracked CVN specimens. *Engineering Fracture Mechanics.* 58, 249-270.

[15] Larsson, S.G and Carlsson, A.J. (1973) Influence of non-singular stress terms and specimen geometry on small scale yielding at crack-tips in elastic-plastic materials. *Journal of Mechanics and Physics of Solids.* 21, 263-277.

[16] Lin, T, Evans, A.G and Ritchie, R.O. (1986) A statistical model of brittle fracture by transgranular cleavage. *Journal of Mechanics and Physics of Solids*, 21, 263-277.

[17] Moinereau, D. (1996) Local approach to fracture applied to reactor pressure vessel, synthesis of a cooperative programme between EF, CEA, Framatome and AEA. *Journal de Physique IV*, 6,243-257.

[18] Mudry, F, Rienzo, F.D and Pineau, A. (1989) Numerical comparison of Global and Local Fracture Criteria in Compact Tension and Center-Crack Panel Specimens. Non-linear Fracture Mechanics, II-Elastic-Plastic Fracture, ASTM STP 995 (Edited by Landes et. al.), *American Society of Testing Materials*, Philadelphia, 24-39.

[19] Mudry, F. (1987) A local approach to cleavage fracture. *Nuclear Engineering and Design.* 105, 65-76.

[20] Minami, F, Bruckner-Foit, A, Munz, D and Trolldenier, B. (1992) Estimation procedure for the Weibull parameters used in the local approach. *International Journal of Fracture.* 54, 197-210.

[21] McMohan, C.L and Cohen, M. (1965) Initiation of cleavage in polycrystalline iron. *Acta Metallurgica.* 13, 591-604.

[22] MSC/PATRAN (2005) MSC Software Inc.

[23] Nevalainen, M and Dodds, R.H. (1995) Numerical investigation of 3-D constraint effects on brittle fracture in SE(B) and C(T) specimens. *International Journal of Fracture.* 74, 131-161.

[24] Rice, J.R. (1968) A path-independent integral and the approximation analysis of strain concentration by notches and cracks, *Journal of Applied Mechanics*, *Transactions ASME*, 35, 379-386.

[25] Ruggieri, C and Dodds, R.H. (1998) Numerical evaluation of probabilistic fracture parameters with WSTRESS. *Engineering Computations.* 15, 49-73.

[26] Ruggieri, C, Dodds, R.H. and Wallin, K. (1998) Constraint effects on reference temperature T_0 for ferritic steels in the transition region. *Engineering Fracture Mechanics.* 60, 19-36.

[27] Ruggieri, C, Minami, F and Toyoda, M. (1995) A statistical approach for fracture of brittle materials based on the chain-of-bundles model. *Jounal of Applied Mechanics*. 62, 320-328.

[28] Ruggieri, C and Dodds, R.H. (1996) A transferability model for brittle fracture including constraint and ductile tearing effects, a probabilistic approach. *International Journal of Fracture*. 79, 309-340.

[29] Rice, J.R. (1974) Limitations to the small scale yielding approximation for crack tip plasticity. *Journal of Mechanics and Physics of Solids*. 22, 17-26.

[30] Sorem, W.A, Dodds, R.H and Rolfe, S.T. (1991) Effects of crack depth on elastic-plastic fracture toughness. *International Journal of Fracture*, 47, 105-126.

[31] Westergaard, H.M. (1939) Bearing pressures and cracks, *Journal of Applied Mechanics*, 6, 49-53.

[32] Wallin, K. (1989) Fracture toughness testing in the ductile-brittle transition region, *Advances in fracture research, Proceedings of the seventh international conference on fracture (ICF 7)*, K. Salama, et. al., Editors, Pergamon press, Oxford, UK, 267-276.

[33] Wallin, K. (1984) The scatter in K_{IC} results, *Engineering Fracture Mechanics*, 19, 1085-1093.

[34] Wallin, K, Sarrio, T and Torronen, K. (1984) Statistical model for carbide induced brittle fracture in steel, *Metal Science*, 18, 13-16.

[35] Wang, Y.Y. (1991) A two-parameter characterization of elastic-plastic crack-tip and applications to cleavage fracture. PhD thesis, Department of Mechanical Engineering, MIT.

[36] Williams, M.L. (1957) On the stress distribution at the base of a stationary crack. *Journal of Applied Mechanics*. 24, 109-114.

[37] Wiesner, C.S and Goldthrope, M.R. (1996) The effect of temperature and specimen geometry on the parameters of the local approach to cleavage fracture. *Journal de Physique IV*, 6,295-304.

[38] Xia, L and Shih, C.F. (1996) Ductile crack growth-III, transition to cleavage fracture incorporating statistics. *Journal of Mechanics and Physics of Solids*. 44, 603-639.

[39] Xia, L and Cheng, L. (1997) Transition from ductile teraing to cleavage fracture, A cell model approach. *International Journal of Fracture*. 87, 289-305.